Pharm Res (2013) 30:1328–1337
DOI 10.1007/s11095-013-0972-0

RESEARCH PAPER

A New Approach to Dissolution Testing by UV Imaging and Finite Element Simulations

Johan P. Boetker • Jukka Rantanen • Thomas Rades • Anette Müllertz • Jesper Østergaard • Henrik Jensen

Received: 16 October 2012 / Accepted: 3 January 2013 / Published online: 11 January 2013

ABSTRACT

Purpose Most dissolution testing systems rely on analyzing samples taken remotely from the dissolving sample surface at different time points with poor time resolution and therefore provide relatively unresolved temporally and spatially information on the dissolution process. In this study, a flexible numerical model was combined with a novel UV imaging system, allowing monitoring of the dissolution process with sub second time resolution.

Methods The dissolution process was monitored by both effluent collection and UV imaging of compacts of paracetamol. A finite element model (FEM) was used to characterize the UV imaging system.

Results A finite element model of the UV imaging system was successfully built. The dissolution of paracetamol was studied by UV imaging and by analysis of the effluent. The dissolution rates obtained from the collected effluent were in good agreement with the numerical model. The numerical model allowed an assessment of the ability of the UV imager to measure dissolution—time profiles. The simulation was able to extend the experimental results to conditions not easily obtained experimentally.

Conclusions Combining FEM,experimental dissolution data and UV imaging provided experimental validation of the FEM model as well as a detailed description of the dissolution process.

KEY WORDS dissolution · finite element method (FEM) · numerical analysis · simulation · UV imaging

J. P. Boetker · J. Rantanen · T. Rades · A. Müllertz · J. Østergaard · H. Jensen (✉)
Department of Pharmacy, Faculty of Health and Medical Sciences
University of Copenhagen, Universitetsparken 2
2100 Copenhagen, Denmark
e-mail: hj@farma.ku.dk

ABBREVIATIONS

A	radius of circular compact
C	concentration
C_{sat}	saturation concentration
d	flow channel width
D	diffusion coefficient
D_H	hydraulic diameter
F	mass flux of dissolving compound
FEM	finite element method
H	characteristic length defined as the height of the flow cell over the compact
J	dissolution rate
Pe	Peclet number
P_s	shear Peclet number
Q	volumetric flow rate
Re	Reynolds number
u	velocity
U	average linear flow rate
USP	United States pharmacopeia
UV	ultraviolet
V_f	volumetric flow rate
v	kinematic viscosity
ρ	density

INTRODUCTION

Dissolution testing is of paramount importance in the drug development process and a key parameter in the characterization of new solid dosage forms (1,2). The key factors describing drug dissolution may be separated into an intrinsic dissolution rate, drug compound solubility and drug transport properties; these parameters will have an impact on the measured overall dissolution rate, but the relative importance may be difficult to quantify for a given solid

dosage form. For this reason dissolution tests are mainly employed in the pharmaceutical industry to evaluate batch to batch consistency within batches and to characterize the dissolution behavior of new chemical entities (3,4). Furthermore, considerable efforts have also been aimed at correlating the *in vitro* dissolution behavior to *in vivo* bioavailability (2,4–9).

Dissolution tests are usually performed in standardized dissolution vessels as specified for example in the United States Pharmacopeia (USP). The two most common dissolution tests (paddle and basket method) are based on the principle of having a solid dosage form in a vessel filled with dissolution medium that is either agitated by a paddle or by rotation of the basket. These dissolution methods have recently been investigated numerically (10–12) resulting in a better understanding of previously unnoticed phenomena. It has for instance been shown that the USP paddle method is impaired by turbulent regimes resulting in highly heterogeneous flow patterns within the dissolution system (11). These heterogeneous flows have subsequently been linked to a high number of failed dissolution tests and product recalls (11). The USP basket method is likewise subjected to chaotic hydrodynamics that are cumbersome to characterize mechanistically (10). Further, the designs of the USP paddle and basket methods prevent detailed observations of the dissolution behavior.

A prerequisite for a complete understanding of dissolution processes is the ability to monitor drug dissolution both at short and long time scales, as well as to have an accurate numerical model for a complete description and quantification. The approach taken in the present work was to utilize dissolution tests endowed with well behaved hydrodynamics. To achieve this goal, a flow cell (depicted in Fig. 1) resembling to some extent the cell described by Nelson and Shah (13) was applied in order to ensure hydrodynamics characterized by laminar flow profiles (13,14). Numerical analysis by Nelson and Shah (13) of laminar flow system has been performed (15–17) and a reasonably good agreement between the simulations and the experimental dissolution rates was achieved (15). Greco *et al.* (18) utilized numerical analysis to describe the velocity profiles within a flow cell that had a design similar to that of Nelson and Shah (13). D'Arcy and Persoons (19) and D'Arcy *et al.* (20) have utilized numerical analysis to investigate the flow behavior in the USP 4 dissolution apparatus.

The recently developed UV imaging technique enables spatially (2D) and temporally resolved imaging of dissolution processes within a flow cell to be performed (21–26). These 2D concentration maps provided by UV imaging have sparked interest in understanding the concentration distributions within the flow cell (since the UV imaging system utilizes this concentration distribution for calculating the dissolution rates). The geometry of this commercially available UV imaging flow cell is more complicated than the previously investigated parallel piped rectangular cells (13,15,18) due to the curved ceiling of the cell (Fig. 1a).

Overall, the present study therefore combines finite element based numerical analysis and UV imaging in a new approach to dissolution testing which successfully enables a detailed description of the dissolution process. Specifically we aim to 1) construct an experimentally and numerically validated quantitative FEM model, 2) evaluate the UV imaging approach for obtaining qualitative and quantitative information on dissolution rate, 3) establish under which conditions more simple analytical dissolutions models may be used as a good approximation and finally to utilize the numerical model for characterizing dissolution at very low flow rates which are not easily obtained experimentally.

MATERIALS AND METHODS

Materials

Paracetamol was obtained from Sigma-Aldrich (batch no. 020 M0203, 98.0–101.0% USP grade). Ultra pure water was obtained from a Millipore Direct-Q UV3 system (Millipore, Billerica, MA, USA).

Methods

UV Imaging Instrumentation

An Actipix SDI300 dissolution imaging system (Paraytec Ltd., York, UK) was used to obtain the UV imaging data. The total imaging area is 9 mm × 7 mm (1,280 × 1,024 pixels). A Xe lamp was utilized as light source. Imaging was performed at a wavelength of 288 and 300 nm. The image acquisition rate was one frame every 2 s. Images were analyzed with Actipix D100 software version 1.3 (Paraytec Ltd.) and Matlab version 7.11.0.584 2010b (Natick, Massachusetts, USA) was used to convert absorbance images into concentration images. The pixels were binned in the horizontal direction in sets of 10 (10 × 1 pixel binning). A syringe pump was used for infusion of the dissolution medium. Further details on the instrumentation have been provided elsewhere (21).

Preparation of Compacts

Compacts were prepared by weighing 15 mg of substance into a stainless steel cylinder (inner diameter: 2 mm) held in a manual press (Actipress, Paraytec Ltd.). A torque screwdriver was used to compress the paracetamol samples at a constant torque (pressure) of 70 cNm.

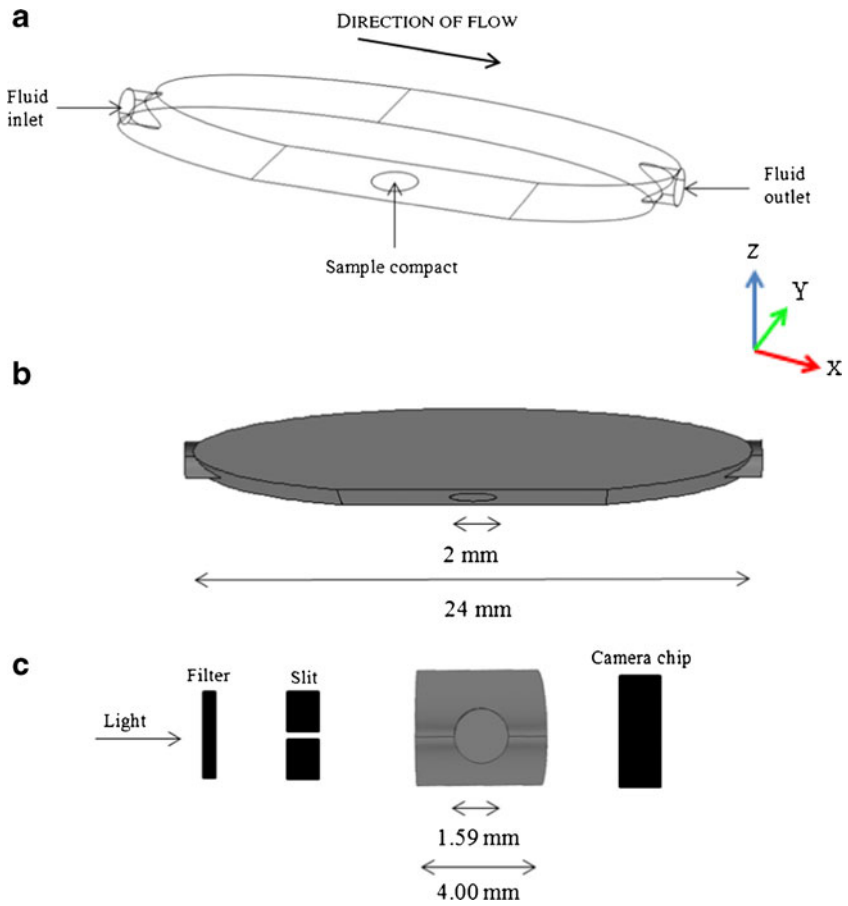

Fig. 1 (**a**) Schematic representations of the UV imaging cell. (**b**) Dimensions of the cell seen from the side. (**c**) Dimensions of the cell seen from the front including schematic position of the wavelength filter, the slit and the camera chip.

Dissolution Experiments

The flow was adjusted to a predetermined inlet velocity ($0.588 \cdot 10^{-3}$, $1.18 \cdot 10^{-3}$, $2.35 \cdot 10^{-3}$, $4.70 \cdot 10^{-3}$, $9.40 \cdot 10^{-3}$, $10.91 \cdot 10^{-3}$, $13.85 \cdot 10^{-3}$ and $16.79 \cdot 10^{-3}$ m/s) equivalent to a volumetric flow rate of $7.00 \cdot 10^{-2}$, $1.40 \cdot 10^{-1}$, $2.80 \cdot 10^{-1}$, $5.60 \cdot 10^{-1}$, 1.12, 1.30, 1.65 and 2.00 ml/min, respectively and three replicate dissolution experiments with UV imaging acquisition were subsequently conducted in 4 to 12 min intervals depending on the flow rate. The sampling of the effluent (0.3 to 0.5 ml volumes) was performed by the end of these intervals in order to ensure that the dissolution from the sample compact boundary had reached steady state. The effluent was quantified using UV spectroscopy. The UV absorbance maps were calculated from the transmittance from each pixel using the Actipix D100 software version 1.3 (Paraytec Ltd.). These absorbance values were subsequently converted into concentration maps utilizing a UV imaging calibration curve constructed from imaging of paracetamol stock solutions infused into the flow through cell. The Actipix software allows calculation of the dissolution rates from the UV images provided that the molar absorbance coefficient can be obtained from Beers law. For paracetamol it proved difficult to apply Beers law for the standard curve obtained at 300 nm because linearity was not achieved. However, at 288 nm these requirements to linearity of the standard curve were met. All UV imaging experiments were conducted at 23 ± 1°C.

Diffusivity of Paracetamol

Taylor dispersion analysis (TDA) (27,28) was used to determine the diffusion coefficient of paracetamol in water. An Agilent ^{3D}CE instrument (Agilent Technologies, Waldbronn, Germany) was used for the measurements. UV detection at 200 nm was applied at two windows along the capillary using an Actipix D100 UV area imager detector (Paraytec Ltd., York, UK) (27). The temperature in the capillary cartridge was 22°C. UV absorbance signals from each of the detection windows were obtained using Actipix control software (version 1.2). The detection windows were 1.5 cm in width and were prepared by burning off the polyimide coating. A fused silica capillary (Polymicro Technologies, Phoenix, AZ, USA) of 90 cm length with an inner diameter of 75 μm and lengths of 30 cm and 50 cm to the center of the first and second detection window, respectively, was used. Hydrodynamic sample introduction (50 mbar for 7 s) was performed and the sample was mobilized using a pressure of 50 mbar ($n=10$). Data analysis was performed using Taylor dispersion theory as described previously (28).

Solubility of Paracetamol

The solubility of paracetamol in water was obtained from solubility experiments ($n=3$) consisting of vials containing Milli-Q water and a surplus of paracetamol. The vials were agitated with magnetic stirring for up to 50 h and the temperature (24°C) was controlled with a water bath. Samples were extracted, filtered and diluted appropriately and the paracetamol concentration was obtained using a conventional double beam spectrophotometer (Evolution 300, Thermo scientific, Madison, Wisconsin, USA). The calculated concentrations were monitored until equilibrium was reached.

UV Spectrophotometry and Quantification of Effluent

Paracetamol concentrations in the effluent samples were determined using a conventional double beam spectrophotometer (Evolution 300, Thermo scientific, Madison, Wisconsin, USA) at 241 nm. A calibration curve with paracetamol concentrations of $11 \cdot 10^{-3}$, $22 \cdot 10^{-3}$, $34 \cdot 10^{-3}$, $44 \cdot 10^{-3}$ and $55 \cdot 10^{-3}$ mol/m^3 was constructed for quantification of the effluent paracetamol concentration ($R^2=0.999$).

Numerical Analysis

The numerical analysis was realized by applying the finite element method (FEM) to the UV imaging setup. COMSOL Multiphysics version 4.2a was utilized to build the inner geometry of the flow through cell, to construct the mesh and to solve the partial differential equation system by use of the direct stationary MUMPS (MUltifrontal Massively Parallel sparce direct Solver). The following boundary conditions were applied to the geometry (Fig. 1):

$$\text{Fluid inlet} \quad u = u_0,\ c = 0 \tag{1}$$

$$\text{Fluid outlet} \quad p_0 = 0 \tag{2}$$

$$\text{Sample boundary} \quad F = k_s \cdot (c_{sat} - c) \text{ or } c = c_{sat} \tag{3}$$

in which u_0 is the flow velocity at the inlet boundary (m/s), u is the flow velocity at an arbitrary point within the geometry, c is the bulk concentration of solute (mol/m^3), p_0 is the pressure at the fluid outlet (Pa), F is the mass flux of the dissolving compound from the sample boundary (mol/m^{2}s), k_s is a flux boundary condition (m/s) which represents the surface kinetics of the dissolution of paracetamol with a default value of unity (15) and c_{sat} is the saturation solubility of paracetamol experimentally determined in agitated vials at 24°C. FEM calculation of the UV imaging setup was solved by the coupling of the laminar flow problem with the transport problem assuming a boundary condition of $c = c_{sat}$ at the sample boundary (Table I). This is equivalent to assuming a high k_s.

The FEM simulations solve a partial differential equation for the flow problem Eq. (4) and thus provide a numerical solution for the flow profile. This flow profile is subsequently coupled to the mass balance Eq. (5).

$$\rho \nabla \cdot u = 0 \tag{4}$$

$$u \cdot \nabla c = \nabla \cdot (D \nabla c) \tag{5}$$

in which ρ denotes the density of the solvent (kg/m^3), u is the velocity (m/s), c is the concentration of species (mol/m^3) and D is the diffusion coefficient (m^2/s) determined by Taylor dispersion analysis (Table I).

The mesh was optimized in order to obtain a high accuracy over the sample compact. A global mesh was applied to the overall geometry with a minimum element size of $7.44 \cdot 10^{-5}$m and a finer mesh with a minimum element size of $7.44 \cdot 10^{-7}$m was subsequently applied to the sample compact boundary thus obtaining the desired high accuracy over the sample compact (with a high number of mesh elements) while limiting the computational demands.

The Reynolds number (Re) in the inlet pipe was calculated according to Eq. (6):

$$Re = \frac{QD_H}{\upsilon A} \tag{6}$$

where Q is the volumetric flow rate (m^3/s), D_H is the hydraulic diameter (m), υ is the kinematic viscosity (m^2/s) and A is the cross sectional area of the pipe (m^2).

A projection coupling operator was used to integrate the solute concentrations in the y direction (Fig. 1). This is necessary because the experimental setup of the UV imager provides solution concentrations, which are averaged across the light path. It is therefore necessary to do this integration to obtain FEM simulation comparable to the UV imaging data. Calculations took 20 h with the utilized mesh and were performed on a conventional HP ProBook 6550b laptop (Hewlett-Packard Company, Palo Alto, California, USA) with a 2.4 GHz CPU processor and 4 GB RAM running on a 64-bit operating system.

Table I Simulation Parameters Excluding the Flow Rates

	Paracetamol ± standard deviation (replicates)
c_{sat}	93.4 ±0.9 mol/m^3 ($n=3$)
D	$6.84 \cdot 10^{-10} \pm 0.05 \cdot 10^{-10}$ m^2/s ($n=10$)
ρ	999 kg/m^3

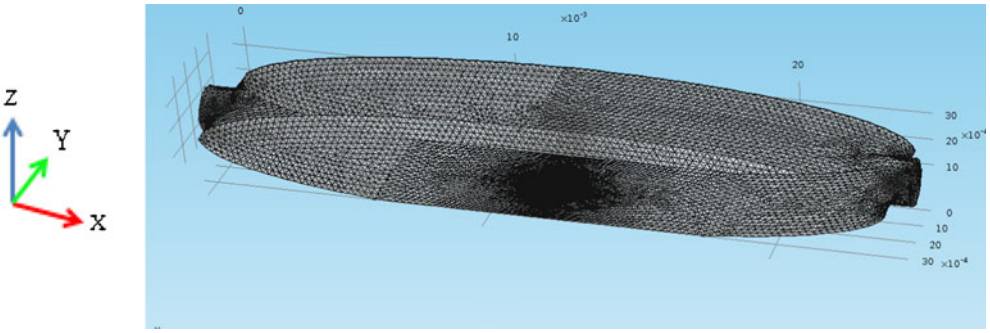

Fig. 2 Meshed geometry of the UV imaging flow cell. The mesh density is highest at the sample compact boundary.

RESULTS AND DISCUSSION

Simulated Flow Profile Within the Cell

Meshing of the UV imaging flow cell was performed with 511.275 mesh elements with the highest mesh density over the sample compact boundary (Fig. 2).

The flow was numerically solved using FEM (Fig. 3). It was, as expected, observed that the maximum flow velocity is inversely proportional to the cross sectional area. Furthermore, at the highest flow rate (2 ml/min) the maximum Reynolds number defined in Eq. 6 was found to be ∽ 27 in the fluid inlet indicating that laminar flow conditions prevail in the UV imaging flow cell.

Dissolution of Paracetamol

The dissolution process of paracetamol was modeled by coupling the solution to the laminar flow with the mass transport equations using the experimentally determined solubility (93.40 mol/m^3) and diffusivity ($6.84 \cdot 10^{-10}$ m^2/s) of paracetamol. The effect of increasing the number of mesh elements was investigated. Figure 4 displays that when the number of mesh elements is raised from 358.224 (FEM coarser mesh) to 386.155 (FEM coarse mesh) and further on to 511.275 (FEM utilized mesh) the FEM calculated dissolution rates converges to the experimentally observed dissolution rates. The number and position of mesh elements is thus a critical parameter that has to be carefully optimized in the FEM calculation. The utilized mesh is observed to provide a sufficient accuracy in the solutions, as further refinement did not improve the accuracy significantly under the present conditions.

A direct comparison between the FEM simulation and the dissolution rates determined from sampling of the effluent was subsequently performed. It is observed from Fig. 4 that the FEM simulation can predict the dissolution of paracetamol from the compact in the flow cell.

Comparison of Concentration Maps from UV Imaging and Simulations

As the FEM model was validated numerically as well as experimentally by comparison with effluent collection data,

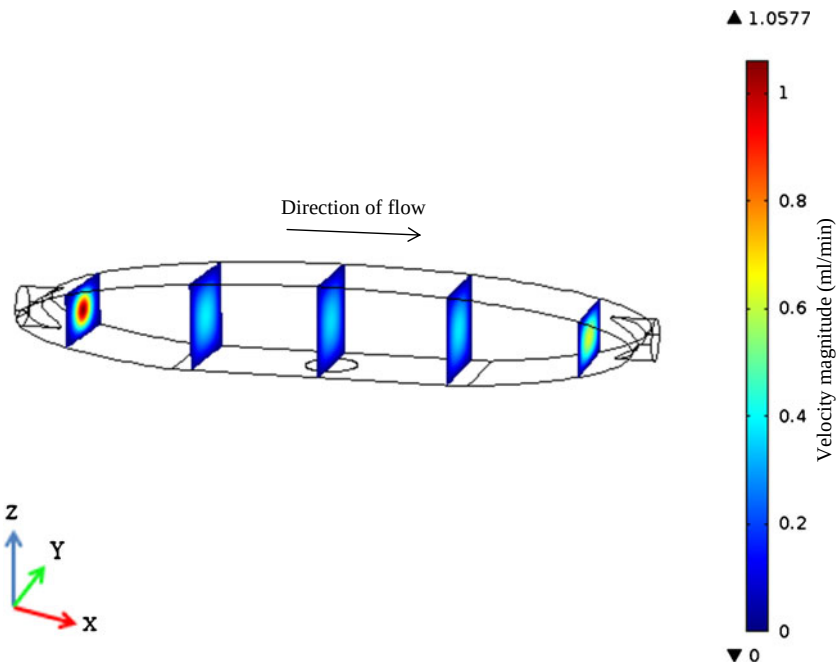

Fig. 3 Simulation of flow profile with a flow rate of $10.91 \cdot 10^{-3}$ m/s.

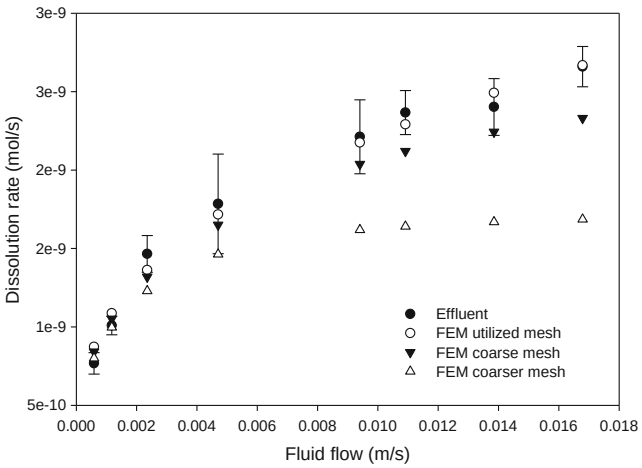

Fig. 4 FEM calculated dissolution rates using different numbers of mesh elements and experimentally obtained effluent dissolution rates of paracetamol. *Error bars* represent the standard deviation ($n = 3$). The experimental data are obtained from sampling and quantification of the effluent.

it may be used to evaluate the UV imaging data. It is observed from Fig. 5 that there is a discrepancy between the FEM simulation and the experimentally obtained UV imaging data. This discrepancy is especially apparent in the vicinity of the sample compact boundary. This phenomenon may be partly caused by the finite size of the pixels (7 by 7 μm^2) in the UV imager, resulting in improper averaging of solute concentrations close to the surface. The mesh element size was 0.7 by 0.7 μm^2 over the sample compact.

The discrepancies with respect to concentrations can be further examined and visualized by comparison of the FEM simulated concentration gradients and the concentration gradients obtained from the UV imaging data. Figure 6a displays a cut plane of the FEM simulation thereby enabling the evaluation of the concentration distributions in this area. A projection operator has been applied to the FEM simulated cut plane (Fig. 6a) which allows a direct comparison of the FEM simulated concentration gradient and the corresponding UV imaging concentration gradient (Fig. 6b). It is observed that the UV imaging system does not obtain the concentration gradient predicted by the FEM simulation (Fig. 6b). This finding is surprising as a recent study on furosemide dissolution suggested a much better ability of the UV imaging system to quantify dissolution rates (29). Still, differences are observed between paracetamol dissolution rates obtained from UV imaging and effluent collection/FEM simulations which suggests that some system parameters of the UV imaging system deserves attention. For example, some of the discrepancy might be explained if the incident light has an angle different from 0° as it can facilitate a higher transmission of light to some parts of the detector (Fig. 6a, dashed line). Non-collimated light may therefore affect

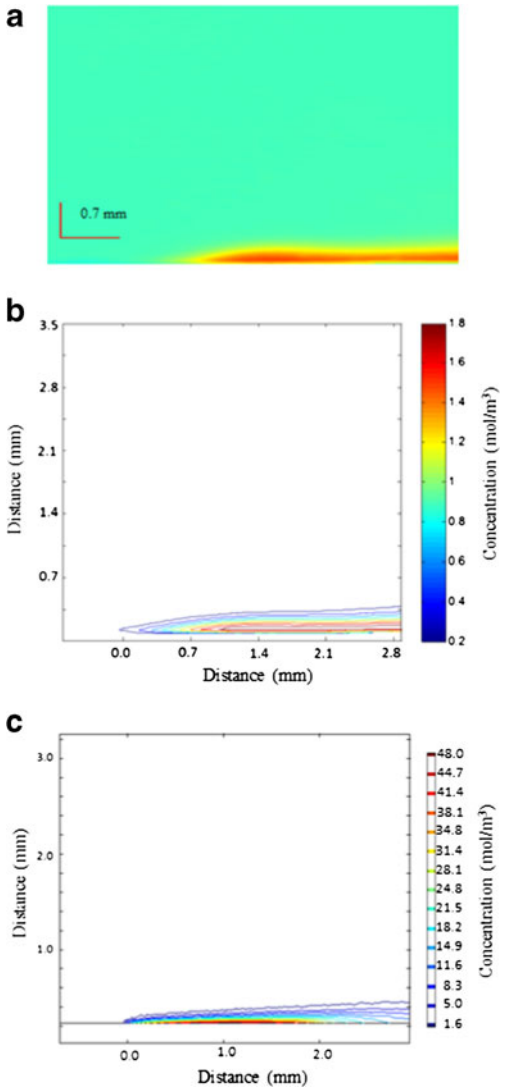

Fig. 5 Color contours depict the concentration in mol/m^3 obtained at 288 nm (**a**) absorbance image of paracetamol dissolution (flow rate $10.91 \cdot 10^{-3}$m/s). (**b**) Concentration image of paracetamol dissolution in water from compact (flow rate $10.91 \cdot 10^{-3}$m/s). (**c**) FEM simulated projection of paracetamol dissolution in water from compact (flow rate $10.91 \cdot 10^{-3}$m/s).

the apparent absorbance of the experimentally observed paracetamol concentrations gradients. Another issue could be related to density gradients formed due to the dissolution of the drug compound. Additional experiments using other model compounds and different flow rates are required in order to have a more complete picture of the ability of the UV-imaging system to quantify dissolution rates.

Analytical Investigations

An interesting attribute of the simulation approach presented here is the possibility of examining a wide range of

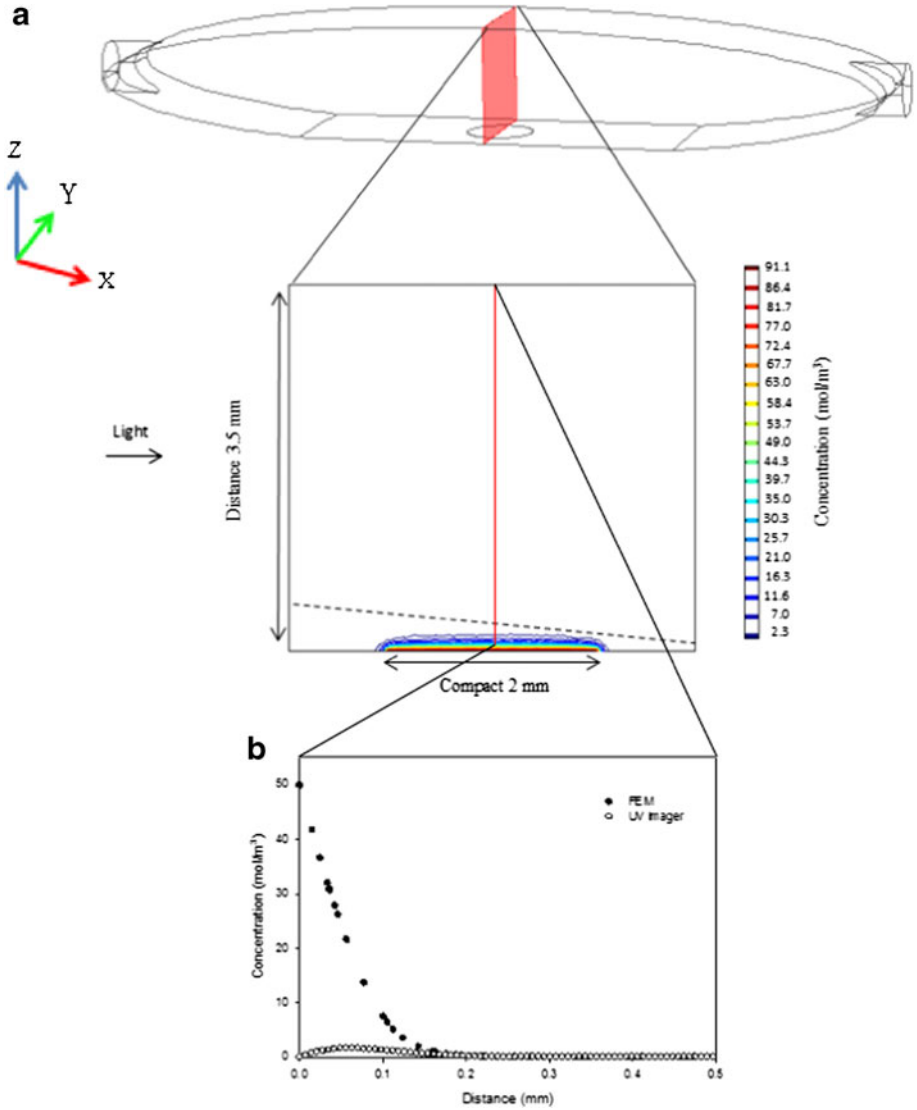

Fig. 6 (**a**) FEM simulations of the UV imaging setup. The significance of the line is explained in the text. (**b**) Projection of the cut plane of the simulation representing the concentration gradient and the corresponding concentration gradient obtained from the UV imager (288 nm wavelength and flow rate $10.91 \cdot 10^{-3}$ m/s).

flow rates. At sufficiently slow flow conditions the paracetamol diffusivity and the flow cell geometry will become the predominant controlling factors for assessment of the dissolution rate. This is observed as a uniform concentration distribution in the z direction of the flow cell (Fig. 7a). This effect is also easily observable by inspection of the simulated dissolution rates (Fig. 7b) where it can be observed that the logarithm of the dissolution rates scale one to one with the logarithm of the flow rate when the flow rate becomes sufficiently low. The relative importance of diffusion and convection may be described by the Peclet number (*Pe*):

$$Pe = \frac{HU}{D} \tag{7}$$

In the present example the transition between drug diffusion/geometry control and fluid dynamic control is seen at an average linear flow rate (U) of approximately 10^{-6} m/s in the inlet (equivalent to 1 ml/day). At this flow rate the *Pe* over the compact can be calculated to be $\backsim 5$ using a characteristic length (H), defined as the height of the flow cell over the compact, of 0.0035 m and the diffusion coefficient (D) of $6.84 \cdot 10^{-10}$ m^2/s. It may therefore be anticipated that conditions corresponding to a *Pe* less than 5 would be best characterized by the dissolution curve below flow rates of 10^{-6} m/s (Fig. 7), whereas conditions corresponding to a *Pe* number higher than 5 would suggest control of the dissolution process by the hydrodynamic flow.

In order to increase the generality of the simulations, the data in Fig. 8b may be converted into a dimensionless form by introducing the Sherwood/Nusselt number (describing a dimensionless flux) for the present compact shape (30). The dissolution rates obtained from the UV imager is also included and a discrepancy between UV imaging dissolution

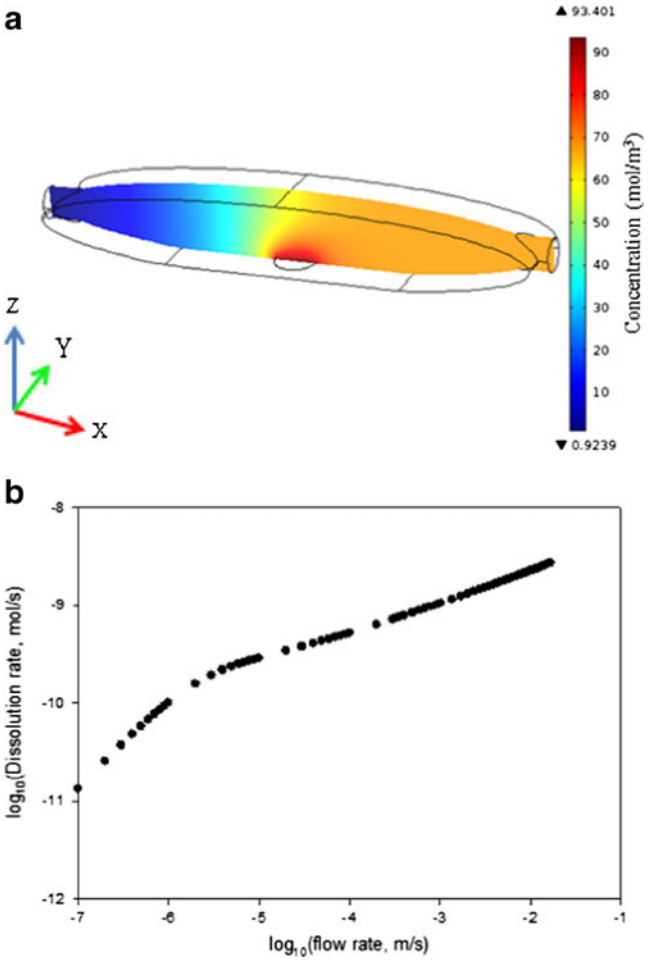

Fig. 7 (**a**) FEM simulation of paracetamol dissolution in the UV imaging setup at a flow rate of $\log_{10}(1 \cdot 10^{-6}\text{m/s})$. (**b**) FEM simulated paracetamol dissolution rates as a function of flow rate.

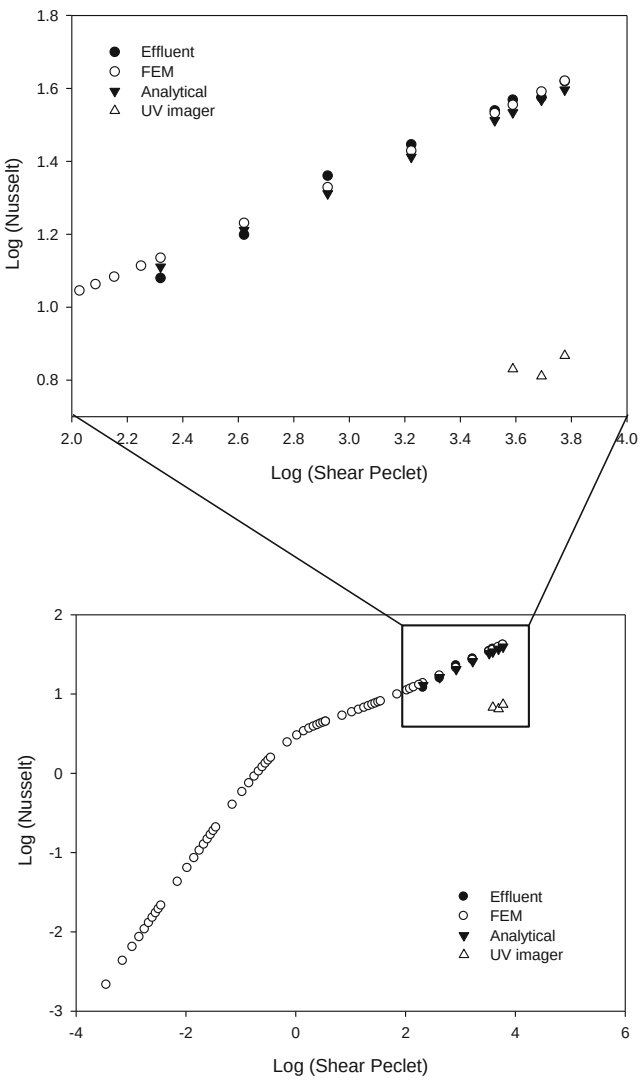

Fig. 8 The logarithmic Nusselt number is plottet against the logarithmic shear Peclet number for the effluent data, FEM solution, UV imaging and the analytical solution using the Stone relationship.

rates and the dissolution rates obtained by FEM simulations and effluent sampling is observed (Fig. 8).

$$Nusselt\ number = \frac{\mathcal{J}}{c_{sat} D A} \tag{8}$$

where $\mathcal{J}$ is the dissolution rate, c_{sat} is the solubility, D is the diffusivity and A is the radius of the circular compact. In Fig. 8 the logarithm of the Nusselt number is plotted against the logarithm of the shear Peclet number (P_s):

$$P_s = \frac{U \cdot A^2}{H \cdot D}; U = \frac{6 \cdot v_f}{H \cdot d} \tag{9}$$

where d is the flow channel width and V_f is the volumetric flow rate. Furthermore, the Stone relationship (Eq. 10) provides an analytical solution for relating the shear Peclet number to the Nusselt number for a circular compact geometry (30). This relationship is only valid for systems with shear Peclet numbers greater than 1:

$$Nusselt\ number = 2.157 \cdot P_s^{\frac{1}{3}} \tag{10}$$

It is observed that a good agreement can be obtained between the analytical Stone relationship, the effluent data and the FEM data (Fig. 8). It is thus stated that if a prior knowledge on diffusivity and solubility of a compound exists it would be possible to calculate the dissolution rate using Eqs. 9 and 10 at a given flow rate assuming a convective diffusion controlled dissolution mechanism. Combining Eqs. 8, 9 and 10 also provides a direct calculation of the dissolution rate in mol/s which has previously been reported by Nelson and Shah (13):

$$\mathcal{J} = 2.157 \cdot D^{\frac{2}{3}} \cdot C_{sat} \cdot A^{\frac{5}{3}} \cdot \left(\frac{6 \cdot v_f}{H^2 \cdot d}\right)^{\frac{1}{3}} \tag{11}$$

However, it should be mentioned that these analytical equations are only valid when certain assumptions holds for

the flow cell. The flow must be laminar, the flow must be sufficiently high so that the upper boundary has no effect on the mass transfer, the shear forces from the solvent flow over the compact surface must be uniform and the diffusion of compound may only occur in the direction that is normal to the surface of the dissolving compact. At the experimental conditions applied most of these assumptions hold for the UV imaging system, however, given the geometry of the flow cell it cannot be claimed that the shear force is uniform over the compact surfaces. The accuracy of the analytical approach was further investigated using Eq. 11 to calculate the dissolution rates at all the given flow rates and comparing these to the FEM calculated dissolution rates. A deviation of up to 5.7% was observed between dissolution rates calculated from Eq. 11 and the dissolution rates obtained from the FEM solutions. These analytical equations may thus be utilized to give an estimate of the dissolution rate for a given compound at a defined flow rate but certain limitations in the accuracy of such calculations may apply.

With the above mentioned limitations for accuracy in mind, it may be argued that if the dissolution rate of a compound deviates substantially from the estimates derived from the analytical Stone relationship, it may be an indication that some other physiochemical phenomena are occurring. Such a phenomenon could be a solid form change, a hydrate formation or a chemical reaction over a finite time interval. If for instance the starting solid form possessed a higher solubility than the thermodynamically assessed c_{sat} value a discrepancy would arise between the experimentally and analytically determined dissolution rates. UV imaging of such systems could be helpful in unraveling the cause of unexpected dissolution behavior (22,23,26).

Finally, at very high flow rates, the overall dissolution may be influenced by the intrinsic dissolution rate (k_s) and the flow may not be laminar. This will manifest itself as deviations from the relationship presented in Fig. 8.

CONCLUSION

Numerical analysis utilizing the finite element method (FEM) was shown to be capable of estimating the dissolution rate of paracetamol within a flow cell at various fluid flow rates. Furthermore, the FEM approach also provided concentration gradients within the flow cell, which were compared to the UV imaging dissolution data. The UV imager provided qualitative information of the dissolution process, but quantification of paracetamol dissolution under the investigated conditions was not possible. Combining FEM and experimental dissolution data obtained from effluent collection form the UV imaging cell allowed experimental validation of the FEM model. The simulation was able to extend the experimental results to conditions at high and, in particular, to low flow rates that are not easily obtained experimentally.

REFERENCES

1. Siewert M, Dressman J, Brown CK, Shah VP. FIP/AAPS guidelines to dissolution/*in vitro* release testing of novel/special dosage forms. AAPS PharmSciTech. 2003;4:E7.
2. Gray V, Kelly G, Xia M, Butler C, Thomas S, Mayock S. The science of USP 1 and 2 dissolution: present challenges and future relevance. Pharm Res. 2009;26:1289–302.
3. Dressman JB, Amidon GL, Reppas C, Shah VP. Dissolution testing as a prognostic tool for oral drug absorption: immediate release dosage forms. Pharm Res. 1998;15:11–22.
4. Tong C, Lozano R, Mao Y, Mirza T, Löbenberg R, Nickerson B, *et al.* The value of *in vitro* dissolution in drug development. Pharm Technol. 2009;33:52–64.
5. Amidon GL, Lennernas H, Shah VP, Crison JR. A theoretical basis for a biopharmaceutic drug classification: the correlation of *in vitro* drug product dissolution and *in vivo* bioavailability. Pharm Res. 1995;12:413–20.
6. Mudie DM, Amidon GL, Amidon GE. Physiological parameters for oral delivery and *in vitro* testing. Mol Pharm. 2010;7:1388–405.
7. Lehto P, Aaltonen J, Tenho M, Rantanen J, Hirvonen J, Tanninen VP, *et al.* Solvent-mediated solid phase transformations of carbamazepine: effects of simulated intestinal fluid and fasted state simulated intestinal fluid. J Pharm Sci. 2009;98:985–96.
8. Wilson D, Wren S, Reynolds G. Linking dissolution to disintegration in immediate release tablets using image analysis and a population balance modelling approach. Pharm Res. 2012;29:198–208.
9. Soto E, Haertter S, Koenen-Bergmann M, Staab A, Troconiz IF. Population *in vitro-in vivo* correlation model for pramipexole slow-release oral formulations. Pharm Res. 2010;27:340–9.
10. D'Arcy DM, Corrigan OI, Healy AM. Evaluation of hydrodynamics in the basket dissolution apparatus using computational fluid dynamics—dissolution rate implications. Eur J Pharm Sci. 2006;27:259–67.
11. Kukura J, Baxter JL, Muzzio FJ. Shear distribution and variability in the USP Apparatus 2 under turbulent conditions. Int J Pharm. 2004;279:9–17.
12. D'Arcy DM, Corrigan OI, Healy AM. Hydrodynamic simulation (computational fluid dynamics) of asymmetrically positioned tablets in the paddle dissolution apparatus: impact on dissolution rate and variability. J Pharm Pharmacol. 2005;57:1243–50.
13. Nelson KG, Shah AC. Convective diffusion-model for a transport-controlled dissolution rate process. J Pharm Sci. 1975;64:610–4.
14. Shah AC, Nelson KG. Evaluation of a convective diffusion drug dissolution rate model. J Pharm Sci. 1975;64:1518–20.
15. Missel PJ, Stevens LE, Mauger JW. Reexamination of convective diffusion/drug dissolution in a laminar flow channel: accurate prediction of dissolution rate. Pharm Res. 2004;21:2300–6.
16. Neervannan S, Reinert JD, Stella VJ, Southard MZ. A numerical convective-diffusion model for dissolution of neutral compounds under laminar-flow conditions. Int J Pharm. 1993;96:167–74.
17. Neervannan S, Dias LS, Southard MZ, Stella VJ. A convective-diffusion model for dissolution of 2 noninteracting drug mixtures from co-compressed slabs under laminar hydrodynamic conditions. Pharm Res. 1994;11:1288–95.
18. Greco K, Bergman TL, Bogner R. Design and characterization of a laminar flow-through dissolution apparatus: comparison of hydrodynamic conditions to those of common dissolution techniques. Pharm Dev Technol. 2011;16:75–87.

19. D'Arcy DM, Persoons T. Mechanistic modelling and mechanistic monitoring: simulation and shadowgraph imaging of particulate dissolution in the flow-through apparatus. J Pharm Sci. 2011;100:1102–15.
20. D'Arcy DM, Liu B, Persoons T, Corrigan OI. Hydrodynamic complexity induced by the pulsing flow field in USP dissolution apparatus 4. Dissolut Technol. 2011;18:6–13.
21. Østergaard J, Meng-Lund E, Larsen SW, Larsen C, Petersson K, Lenke J, *et al.* Real-time UV imaging of nicotine release from transdermal patch. Pharm Res. 2010;27:2614–23.
22. Østergaard J, Ye F, Rantanen J, Yaghmur A, Larsen SW, Larsen C, *et al.* Monitoring lidocaine single-crystal dissolution by ultraviolet imaging. J Pharm Sci. 2011;100:3405–10.
23. Boetker JP, Savolainen M, Koradia V, Tian F, Rades T, Müllertz A, *et al.* Insights into the early dissolution events of amlodipine using UV imaging and raman spectroscopy. Mol Pharm. 2011;8:1372–80.
24. Ye FB, Yaghmur A, Jensen H, Larsen SW, Larsen C, Ostergaard J. Real-time UV imaging of drug diffusion and release from Pluronic F127 hydrogels. Eur J Pharm Sci. 2011;43:236–43.
25. Pajander J, Baldursdottir S, Rantanen J, Ostergaard J. Behaviour of HPMC compacts investigated using UV-imaging. Int J Pharm. 2012;427:345–53.
26. Hulse WL, Gray J, Forbes RT. A discriminatory intrinsic dissolution study using UV area imaging analysis to gain additional insights into the dissolution behaviour of active pharmaceutical ingredients. Int J Pharm. 2012;434:133–9.
27. Ostergaard J, Jensen H. Simultaneous evaluation of ligand binding properties and protein size by electrophoresis and Taylor dispersion in capillaries. Anal Chem. 2009;81:8644–8.
28. Ye FB, Jensen H, Larsen SW, Yaghmur A, Larsen C, Ostergaard J. Measurement of drug diffusivities in pharmaceutical solvents using Taylor dispersion analysis. J Pharm Biomed. 2012;61:176–83.
29. Gordon S, Naelapää K, Rantanen J, Selen A, Müllertz A, Østergaard J. Real-time dissolution behavior of furosemide in biorelevant media as determined by UV imaging. Pharm Dev Technol. doi:10.3109/10837450.2012.737808.
30. Zhang W, Stone HA, Sherwood JD. Mass transfer at a microelectrode in channel flow. J Phys Chem-Us. 1996;100:9462–4.